Acta Mech 228, 2413–2427 (2017)
DOI 10.1007/s00707-017-1828-1

ORIGINAL PAPER

Fernando Calvo · Antonio Bula · Leonardo Di Mare · Samira Garcia

CFD simulation of multiphase (liquid–solid–gas) flow in an airlift column photobioreactor

Received: 1 February 2016 / Revised: 10 February 2017 / Published online: 28 March 2017
© Springer-Verlag Wien 2017

Abstract A 2D computational fluid dynamics simulation was carried out using a multiphase flow model with an Eulerian–Eulerian approach for a microalgae culture in an airlift column photobioreactor. Simulation was performed for a $0.0625\, l/l_{\text{culture}} \cdot \text{min}$ inlet airflow. Air, water and microalgae velocity contours showed less gas phase present in the downcomer than in the riser, suggesting the necessity of vigorous mixing in the ascendant portion if homogeneous water and solid flow is to be achieved. Air velocity is smaller in the downcomer (shorter velocity vectors) than in the riser. Water velocity vectors point always in the expected direction, down in the downcomer and up in the riser. Microalgae paths, perhaps due to the small size of the microorganisms, follow the water velocity vectors. As there are fewer hydraulic restrictions to the liquid phase in the riser, a large amount of energy is dissipated by gas–liquid interactions. In the downcomer region, the gas phase is almost nonexistent, and bubble collisions are almost nonexistent as well. A quasi-stagnation zone was found at the lower section of the downcomer, showing that the design requires improvement. Finally, the turbulent kinetic energy is larger at the top and middle region of the riser; meanwhile, it is lower at the downcomer. Similar results were observed for the energy dissipation rate.

List of symbols

d_{B}	Bubble diameter
d_{M}	Microalgae diameter
g	Gravity
$\mathbf{M}_{\text{I},\alpha}$	Momentum force at the interphase for α phase
P_α	Turbulent kinetic energy production term
Pr_{t}	Turbulent Prandtl number

F. Calvo
Mechanical Engineering Department, Universidad Pontificia Bolivariana, Cra. 6 No. 97 A–99, Montería, Colombia
E-mail: fernando.calvos@upb.edu.co

A. Bula (✉) · L. Di Mare · S. Garcia
Mechanical Engineering Department, Universidad Del Norte, Km 5 Antigua Vía Puerto Colombia, Barranquilla, Colombia
E-mail: abula@uninorte.edu.co

L. Di Mare
E-mail: ldimare@uninorte.edu.co

S. Garcia
E-mail: sfreites@uninorte.edu.co

r	Volume fraction
t	Time
u	Phase velocity

Greek symbols

α	Phase (liquid/gas/solid)
ε	Turbulence energy dissipation rate
k	Turbulence kinetic energy
ρ	Density
∇P	Pressure gradient
μ	Viscosity
$\mu_{g,l}$	Bubble-induced liquid viscosity
$\mu_{s,l}$	Solid-particle-induced liquid viscosity
μ_t	Turbulent viscosity
Γ_α	Dispersion Coefficient

Subscripts

l	Liquid phase
g	Gas phase
s	Solid phase
eff	Effective
I	Interphase force
D	Draft
L	Lift
VM	Virtual mass
TD	Turbulent dispersion

1 Introduction

Photobioreactors (PBRs) could be defined as closed systems where microorganisms (commonly microalgae) are able to carry out the photosynthesis process using artificial light, solar light or both of them [1]. PBRs have been widely used for microalgae cultivation [2], since this technology minimizes contamination risks of the culture, improves the reproducibility of culture conditions, provides control over hydrodynamics and temperature and allows appropriate technical design [3]. Particularly, airlift PBRs allow rapid mixing while producing weak shear stress, which makes them suitable for microalgae cultures [4]. Airlift column reactors are widely used in chemical, petrochemical and bioprocess industries because of their simple construction, inexpensive operation, design flexibility, low power requirements, and good mass and heat transfer [5,6]. In this type of equipment, pneumatic mixing is employed to equally and periodically convey all the cells from the lightened zones of the PBR to the dark area [7].

During the operation of an airlift PBR, fluid in the vessel splits into two interconnected zones using a draft tube (riser) as a separating baffle [8], an ascending body (in the riser) and a descending one (in the downcomer), zones 2 and 3 in Fig. 1, respectively. Zone 1 corresponds to the system gas-phase inlet. Because of the previously mentioned advantages of PBRs, several studies have been developed over the last decades. Nevertheless, a better understanding of their hydrodynamic behavior is still a key issue for improving their performance in microalgae cultivation. Both empirical and computational research may contribute to this process. In computer simulation studies, computational fluid dynamics (CFD) techniques have been on the forefront in designing PBRs where microalgae are cultivated [2].

Computational fluid dynamics have made a huge impact in characterization of flow fields in PBRs, becoming a powerful tool for performance prediction, and possibly in design optimization. This could lead to reductions in both resource demand and cultivation time [9].

This study aims to characterize the behavior of various hydrodynamic variables affecting the turbulent multiphase flow (water–air–microalgae) in an airlift PBR through the use of a CFD software under an Eulerian reference frame. Results will be used in the operational optimization of PBRs for microalgae culture.

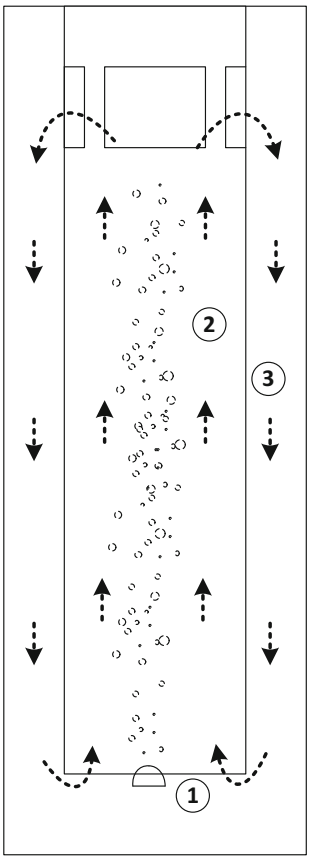

Fig. 1 Airlift PBR operational scheme

2 Model description

As previously mentioned, an Eulerian approach was employed for modeling the described multiphase system. In this method, continuous and dispersed phases are both mathematically modeled as interpenetrating fluids, represented by sets of mass, momentum and energy balances [10]. This approach has some advantages in modeling dispersed phases since the volume fraction of particles (solids phase) or/and bubbles (gas phase) is significant, and they must be accounted for. Moreover, because of its relative simplicity, it has lower computational cost compared to the Lagrangian particle tracking method [11].

Some assumptions taken for this model are listed below [12]:

- All phases are modeled as interpenetrating continua. The probability of any phase presence in the multiphase flow field is given by the instantaneous volume fraction of that phase at that point. The total sum of all volume fractions at any given point, thus, should be unity.
- Liquid and gas phases are treated as incompressible with the same pressure field: $p = p_l = p_g$
- The gas phase is assumed to consist of spherical bubbles of the same size.
- Mass exchange between phases is neglected.
- The whole fluid domain is assumed to be under isothermal condition; thus, heat exchange is not considered.
- Microalgae (the dispersed solid phase) are modeled as spherical solid particles with constant diameter.

The multiphase model solved is comprised by conservation equations for mass, momentum and energy for each phase. Phase interaction models are provided to define the influence that each phase exerts upon another across the interfacial area between them. Mass conservation is defined by

$$\begin{aligned} &\tfrac{\partial}{\partial t}\left(r_\alpha \rho_\alpha\right) + \nabla \cdot \left(r_\alpha \rho_\alpha \vec{u}_\alpha\right) = 0 \\ &(\alpha = l, g, s)\,, \end{aligned} \tag{1}$$

where the volume fraction restriction for the three phases is specified as:

$$\sum r_\alpha = 1. \tag{2}$$

Momentum conservation is presented in Eq. (3):

$$\frac{\partial}{\partial t}\left(r_\alpha \rho_\alpha u_\alpha\right) + \nabla \cdot r_\alpha \rho_\alpha u_\alpha u_\alpha = -r_\alpha \nabla P + r_\alpha \rho_\alpha g + \nabla \cdot \left(r_\alpha \mu_{\alpha,\text{eff}} \left(\nabla u_\alpha + \nabla u_\alpha^T\right)\right) + M_{\text{I},\alpha}. \tag{3}$$

The effective viscosity ($\mu_{\alpha,\text{eff}}$) term includes contributions from molecular viscosity (μ_α) and turbulent dynamic viscosity (μ_α^{T}) [11]. For the liquid phase, the effective viscosity is defined as [13]

$$\mu_{\text{l,eff}} = \mu_\text{l} + \mu_\text{l}^{\text{T}} + \mu_{\text{g,l}} + \mu_{\text{s,l}}. \tag{4}$$

For dispersed phases:

$$\mu_{\text{g,eff}} = \mu_\text{g} + \mu_\text{g}^{\text{T}}, \tag{5}$$

$$\mu_{\text{s,eff}} = \mu_\text{s} + \mu_\text{s}^{\text{T}}. \tag{6}$$

The turbulent viscosity for the liquid phase is computed as:

$$\mu_\text{l}^{\text{T}} = \rho_\text{l} C_\mu \left(\frac{k^2}{\varepsilon}\right), \tag{7}$$

$$\mu_{\text{g,l}} = \rho_\text{l} C_{\mu\text{p}} \varepsilon_\text{g} d_\text{B} \left|u_\text{g} - u_\text{l}\right|, \tag{8}$$

$$\mu_{\text{s,l}} = \rho_\text{l} C_{\mu\text{p}} \varepsilon_\text{s} d_\text{M} \left|u_\text{s} - u_\text{l}\right|. \tag{9}$$

For dispersed phases, the turbulent viscosity is calculated as:

$$\mu_\text{g}^{\text{T}} = \frac{\rho_\text{g}}{\rho_\text{l}} \mu_{\text{T,l}}, \tag{10}$$

$$\mu_\text{s}^{\text{T}} = \frac{\rho_\text{s}}{\rho_\text{l}} \mu_{\text{T,l}}. \tag{11}$$

This model for viscosity was proposed by Jakobsen et al. In his paper "Modeling of Vertical Bubble-Driven Flows", quoted by Wang et al. [13], the effective liquid phase viscosity takes into account not only the liquid own viscosity (μ_l) but also components induced by the turbulence (μ_l^{T}), by the bubbles ($\mu_{\text{g,l}}$) and by the solid phase ($\mu_{\text{s,l}}$). He made a similar analysis for every phase component.

The ($M_{\text{I},\alpha}$) term takes into account the interphase momentum transfer between different phases due to interfacial forces [14], including drag force (M_D), lift force (M_L), virtual mass force (M_VM) and turbulent dispersion force (M_TD):

$$M_\text{I} = M_\text{D} + M_\text{L} + M_\text{VM} + M_\text{TD}. \tag{12}$$

Interfacial forces between two phases were equal and opposite [13]:

$$M_{\text{I,lg}} = -M_{\text{I,gl}}, \tag{13}$$

$$M_{\text{I,ls}} = -M_{\text{I,sl}}. \tag{14}$$

The standard $\kappa-\varepsilon$ turbulent model is used in the current study. The equations employed were developed by Jones and Launder [15] with coefficients suggested by Launder and Sharma [16]. The equations for turbulent kinetic energy and turbulent dissipation, describing multiphase flow, are, respectively [14]:

$$\frac{\partial}{\partial t}\left(r_\alpha \rho_\alpha \kappa_\alpha\right) + \nabla \cdot \left(r_\alpha \rho_\alpha \kappa_\alpha u_\alpha\right) - \nabla \cdot \left(r_\alpha \left(\mu_\alpha + \frac{\mu_\alpha^{\text{T}}}{\sigma_k}\right) \nabla k_\alpha\right) = -r_\alpha \left(P_\alpha - \varepsilon_\alpha \rho_\alpha\right), \tag{15}$$

$$\frac{\partial}{\partial t}\left(r_\alpha \rho_\alpha \varepsilon_\alpha\right) + \nabla \cdot \left(r_\alpha \rho_\alpha \varepsilon_\alpha u_\alpha\right) = \nabla \cdot \left(r_\alpha \left(\mu_\alpha + \frac{\mu_\alpha^{\text{T}}}{\sigma_\varepsilon}\right) \nabla \varepsilon_\alpha\right) + r_\alpha \frac{\varepsilon_\alpha}{k_\alpha} \left(C_{\varepsilon 1} P_\alpha - C_{\varepsilon 2} P_\alpha \varepsilon_\alpha\right), \tag{16}$$

Table 1 Constants used in the $\kappa - \varepsilon$ turbulence model

$C_{\varepsilon 1}$	$C_{\varepsilon 2}$	C_{μ}	$C_{\mu \mathrm{p}}$	σ_{k}	σ_{ε}	Pr_{t}
1.44	1.92	0.09	0.06	1.0	1.3	1.0

where the production term is defined as:

$$P_{\alpha} = \mu_{\alpha}^{\mathrm{T}} \nabla u \cdot \left(\nabla u + \nabla u^{\mathrm{T}} \right) - \frac{\mu_{\alpha}^{\mathrm{T}}}{\rho Pr_{\mathrm{t}}} g \cdot \nabla \rho. \tag{17}$$

The turbulent dispersion term it modeled as [17]:

$$S_{\alpha} = \nabla \left(\Gamma_{\alpha} \cdot \nabla r_{\alpha} \right) = \nabla \left(D_{\alpha} \cdot \nabla \left(\rho_{\alpha} r_{\alpha} \right) \right), \tag{18}$$

$$\Gamma_{\alpha} = \frac{\mu_{\alpha}^{\mathrm{T}}}{Pr_{\mathrm{t}}}. \tag{19}$$

The previously described equations are solved using STAR CCM+®. Constants used to close the model by the software are listed in Table 1 [14].

3 Computational model configuration

Figures 2 and 3 show the airlift PBR and the CAD generated with dimensions already introduced [11].

The analyzed PBR consists of two concentric cylinders made of acrylic material. The outer cylinder is 4 mm thick, 750 mm high and has 250 mm external column diameter. The inner cylinder (riser) is 4 mm thick, 690 mm high and has 150 mm inner diameter. The inner cylinder hangs from the top of the outer one and has 4 windows located near its upper portion to allow water recirculation. During the CAD generation, a modification

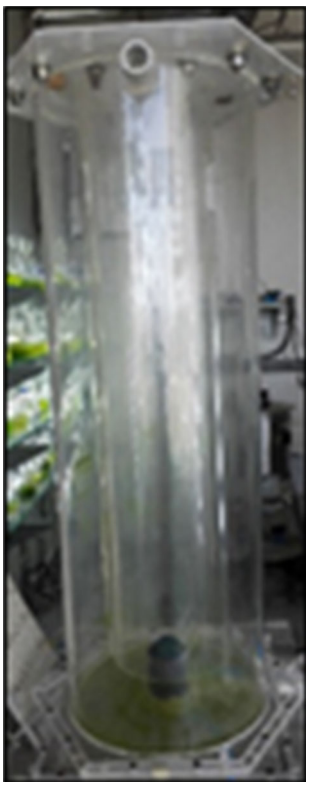

Fig. 2 Modeled airlift PBR

Fig. 3 CAD for photobioreactor

Table 2 Reference values for grid construction

Base size	5×10^{-3} m
Maximum cell size	0.5 m
Number of prism layers	5
Prism layers stretching	1.5
Surface growth rate	1.3

was made to the original PBR. Since the water level does not reach the top of the vessel, CAD's top boundary was set close to the middle of the circulation windows. Air inlet was modeled as a 40-mm-diameter semi sphere. As a first modeling step, a volumetric mesh was generated using the parameters presented in Table 2.

The selected meshing model uses a predominantly hexahedral mesh. It is efficient for filling large volumes and uses less memory per cell than the polyhedral mesh [18]. The volumetric mesh was the basis for establishing the 2D computational domain. It is important to say that the two-dimensional modeling was chosen because previous results [11] show a lack of axial symmetry in the flow when the riser is employed. Figure 4 shows the final grid used.

A grid independence analysis was performed using different base sizes for the mesh elements. Values ranging between 4×10^{-3} and 8×10^{-3} m were used. Resulting values for pressure and velocity of each of the three phases in a given point (in the center of the riser) were compared. The maximum variation found was 4% for water and solid velocities. The values remain essentially the same for mesh sizes of 7×10^{-3} m and smaller. For this reason, a mesh size of 5×10^{-3} m was selected. Table 3 shows the results for different mesh sizes checked.

A summary of the final statistics for the two-dimensional grid is listed in Table 4.

An Eulerian reference frame is used for modeling all phases. The physics of the problem is modeled considering constant density for the phases and $\kappa - \varepsilon$ turbulence model. These models are used for describing each one of the phases in the present study.

Cells were considered as solid spherical particles with a density value similar to that of the water. Freshwater *Chlorella vulgaris* was the microalgae species chosen for the simulation. Cell size for this type of microorganism ranges typically between 5 and 10 μm [19]; therefore, the cell diameter was set to 10 μm. The

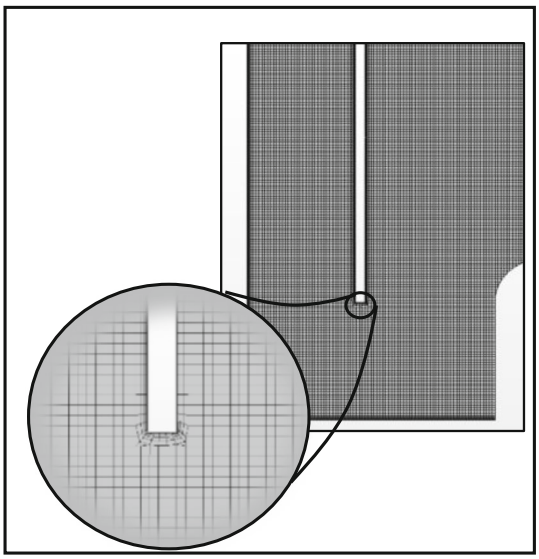

Fig. 4 2D final mesh

Table 3 Velocity dependence on chosen mesh size

Grid base size (mm)	Nodes (N)	Pressure (kPa)	Water vel (m/s)	Air vel (m/s)	Microalgae vel (m/s)
4	177,963	101,322.8	0.242	0.592	0.242
5	116,883	101,323.2	0.241	0.592	0.241
6	82,437	101,324.2	0.238	0.588	0.238
7	62,260	101,322.9	0.242	0.592	0.242
8	48,019	101,329.1	0.239	0.589	0.239
9	39,767	101,321.7	0.234	0.584	0.233

Table 4 Mesh final statistics

Cells	Triangular	26
	Quadrilateral	115,129
	Polygonal	24
	Total	115,179
Total faces		228,653
Total vertices		116,883
Grid base size		4×10^{-3} m

Table 5 Physical properties for the different phases

Continuum properties	Density (kg/m^3)	Dynamic viscosity (Pa-s)	Diameter (m)
Water	997.561	8.8871e−4	N/A
Air	1.18415	1.85508e−5	0.004
Microalgae	1040 [20]	1.0E−6	1e−5

bubble diameter was specified at a value of 4 mm. Table 5 shows modeling properties for water, air bubbles and microalgae. On the other hand, interaction between air bubbles and water considered drag, lift, virtual mass and turbulent dispersion forces. Regarding the interaction between water and microalgae, drag force and turbulent dispersion force were considered. In the present study, drag coefficient is defined by the Schiller–Naumann correlation.

Initial condition for water and microalgae velocity was established as 0 m/s, since both phases are considered stationary at the beginning of the simulation, and no air was considered in the system when the simulation started. Initial volume fractions for microalgae and water were 0.0002 and 0.9998, respectively. This corresponds to a microalgae concentration of 4×10^5 cells/ml. Air velocity was determined from the volumetric

Table 6

Time step (s)	Pressure (kPa)	Water vel. (m/s)	Air vel. (m/s)	Microalgae vel. (m/s)
0.1	101,323.2	0.241	0.592	0.241
0.12	101,323.2	0.241	0.592	0.241
0.14	101,323.3	0.242	0.592	0.241
0.16	101,323.1	0.241	0.591	0.241
0.18	101,322.4	0.245	0.595	0.245

flow rate ($0.0625\,l/l_{culture} \cdot min$). The system is open to the atmosphere, whose pressure is considered to be 101.325 kPa.

Three boundary conditions are identified in the PBR: inlet, outlet and walls. Inlet condition was placed at the sparger's surface, specifying the air velocity. Air volume fraction at the inlet is set to one since only the gas phase goes into the system. The outlet boundary is placed at the top of the PBR. At this section, the impermeable condition is specified for microalgae and water; therefore, only the gas phase leaves the PBR through this boundary. The wall boundary condition is specified in the walls of the PBR.

A total of 30 s were considered for the transient simulation in order to achieve permanent condition. The simulation was performed with a constant time step of 0.1 s. To determine this time step, an analysis similar to that used for the grid independence was accomplished. Time step values in the range from 0.1 to 0.18 s were used. Final velocity results, after 30 s of simulation, were compared in the same domain point. Results are listed in Table 7.

As results turned out to be almost identical, the shorter value was chosen in order to better capture the fast-changing transient process at the beginning of the simulation.

4 Results

Modeling was performed with the chosen parameters. After 30 s of simulation, the water flow pattern is developed and the air plume oscillates permanently inside the photobioreactor. Regarding the microalgae, their flow pattern shows similar characteristics as those developed by the water phase.

4.1 Air and microalgae volume fraction contours

Figures 5 and 6 show the results obtained for air and microalgae volume fraction, respectively. In Fig. 5, it is clear that the air phase is present mainly at the riser zone of the PBR. Air volume fraction around the sparger reaches the highest value, while in the downcomer it is close to zero, as expected, since most of the bubbles entering the PBR leave the system through the top of the equipment. From microalgae volume fraction contours, the mixing effect caused by the air phase can be seen. The presence of microalgae in the whole extension of the PBR is evident, which is desired, as mentioned before. However, the results show zones with a higher presence of the microorganism. That is a consequence of the low velocity in the bottom section of the downcomer, compared to both the riser and the upper part of the downcomer [10].

4.2 Water, air and microalgae volume fraction contours

Comparing air volume fraction contours and air velocity contours, a parallel behavior is evident as observed in Figs. 5, 6 and 7. The highest velocity values are found in the lower and middle sections of the riser, where the volume fraction for the air phase shows its highest values as well. This result is comparable with the study of García et al. [11] where a simulation for an airlift PBR with two phases was performed (air–water). Nevertheless, the presence of the third phase (microalgae) leads to a shorter zone with the maximum velocity for air. In this study, it was seen until the middle of the riser, while in some other studies [11] it is found that this zone extends practically through the entire riser.

Water and microalgae velocity contours are presented in Figs. 8 and 9. As well as for the air phase, water and microalgae present higher values of velocity in the riser than those seen in the downcomer.

These contours show that water recirculates in the PBR through the windows at the top of the riser, at low velocity values. On the other hand, microalgae velocity contours show a similar pattern to that of water, following liquid flow. This is in accordance with the experimental results from Luo and Al-Dahhan [12].

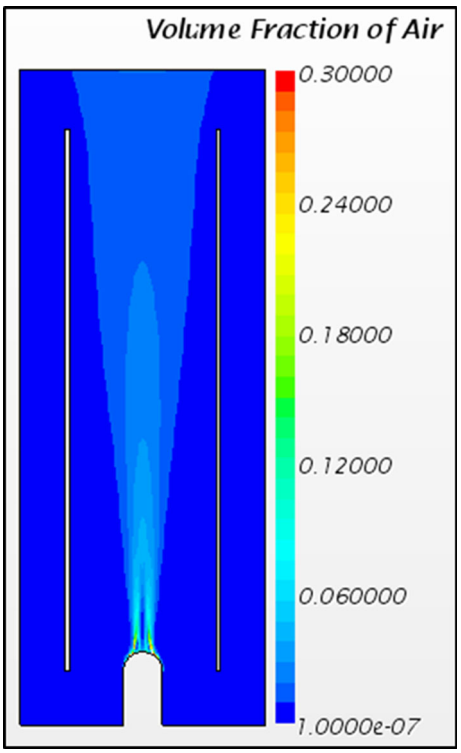

Fig. 5 Air volume fraction contours

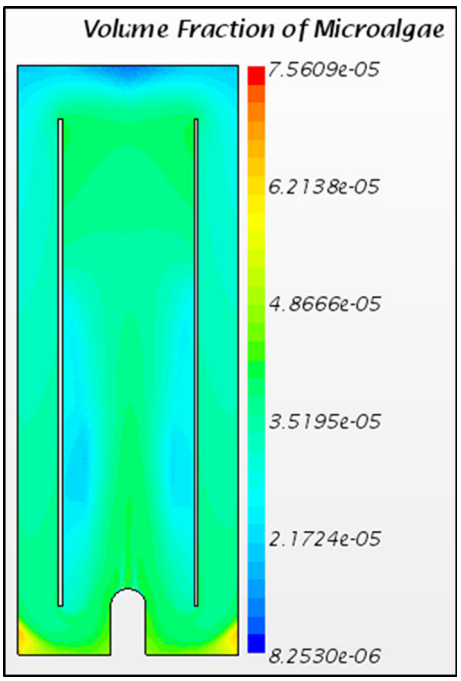

Fig. 6 Microalgae volume fraction contours

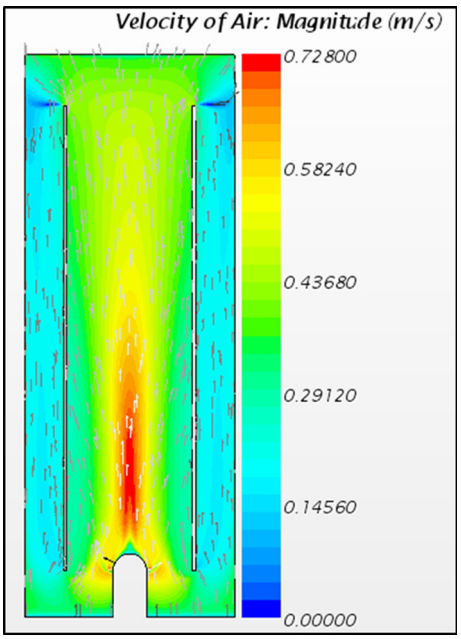

Fig. 7 Air velocity contours and velocity vectors

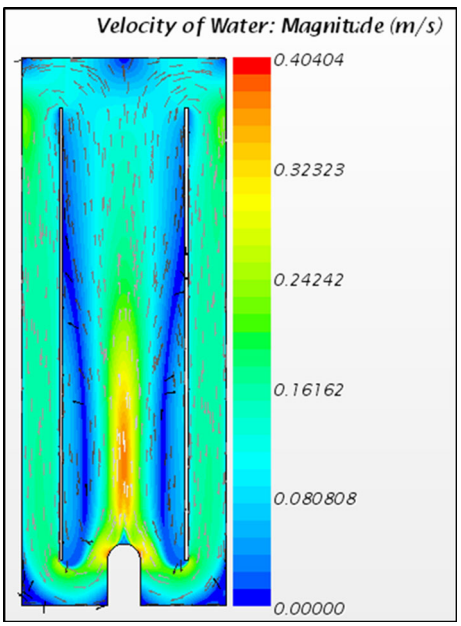

Fig. 8 Water velocity contours and velocity vectors

4.3 Water, air and microalgae velocity vectors

The permeability condition for the air phase at the top of the PBR could be verified with the behavior of the velocity vectors. Figure 7 shows air velocity vectors going out from the system as expected due to the specified boundary condition.

By using this outlet condition, most of the air mass flow entering the system will leave the PBR through the upper surface, thus achieving the mass balance. Nevertheless, some velocity vectors are present in the downcomer, which indicates that some air mass is dragged by the water [11].

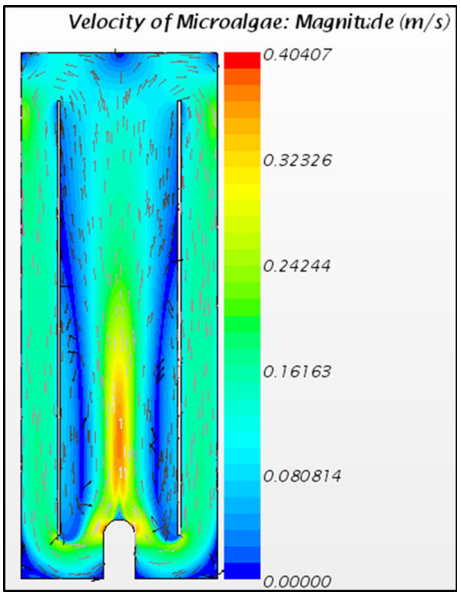

Fig. 9 Microalgae velocity contours and velocity vectors

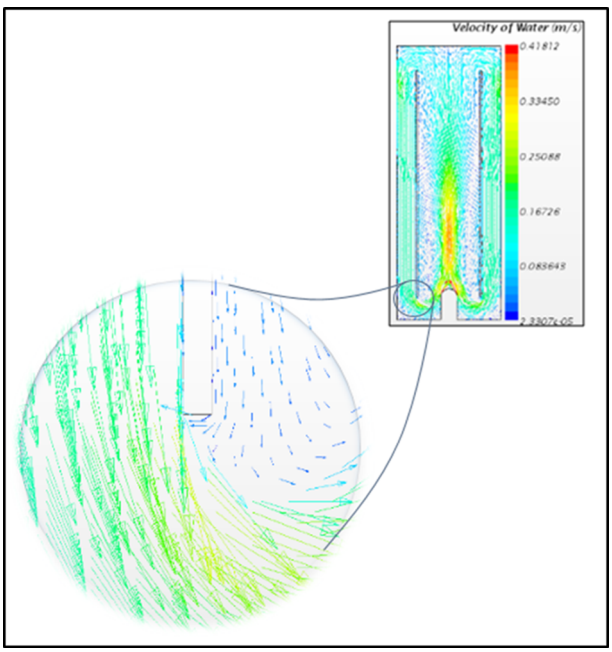

Fig. 10 Water velocity vectors at the bottom of the PBR

Velocity vectors for the water phase are shown in Fig. 8. These vectors are well organized, pointing down in the downcomer and up in the riser, indicating a good mixing performance at the specific volumetric flow rate of air ($0.0625\,\mathrm{l/l_{culture} \cdot min}$). Velocity vectors for microalgae indicate that this dispersed phase follows the flow pattern of the continuous phase, driving the microalgae to constant circulation inside the photobioreactor. Figure 9 shows the velocity vectors for this phase, which are quite similar to those of the water.

As water circulates from the downcomer to the riser, low-pressure zones are expected to be generated producing a backflowing effect in those points. This is validated by water velocity vectors. In Fig. 10, it is noticed that some vectors in the low part of the PBR have a direction contrary to that of the main flow.

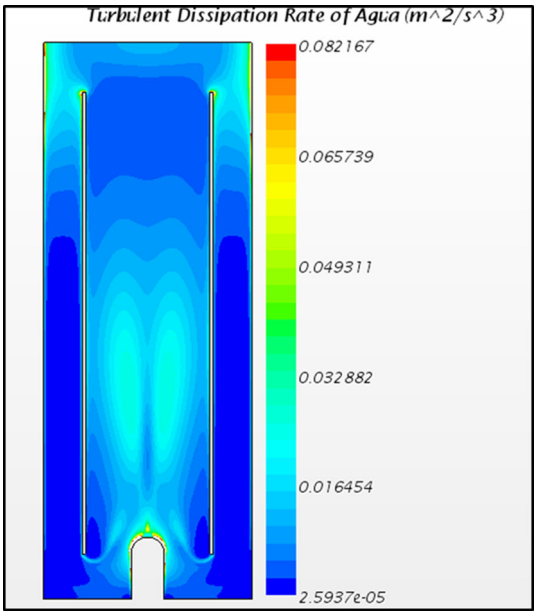

Fig. 11 Water turbulent dissipation rate contours

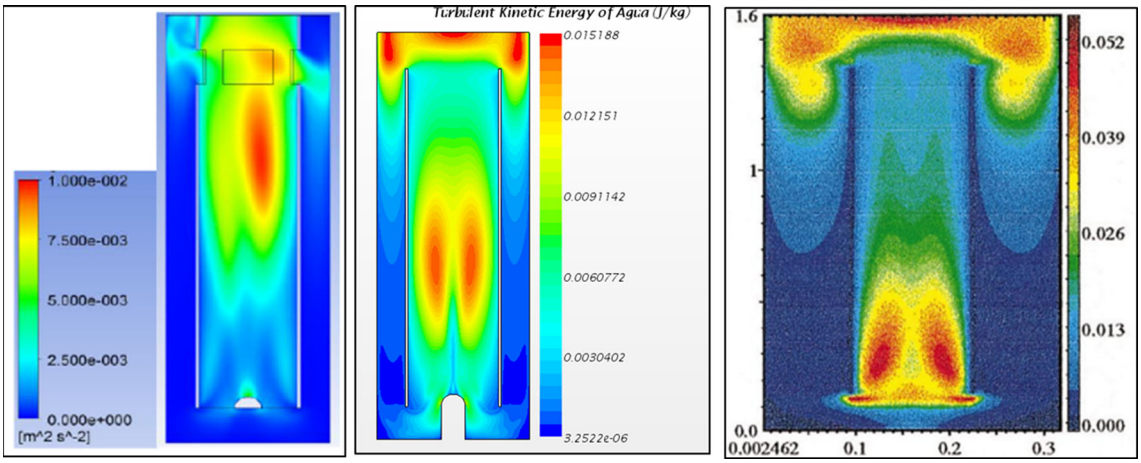

Fig. 12 Water turbulent kinetic energy contours. García et al. [11] (*left*), current investigation (*center*), Oey et al. [10] (*right*)

4.4 Turbulent dissipation rate and kinetic energy for continuous phase

Turbulent dissipation rate and turbulent kinetic energy for the water phase are derived directly from the turbulence model ($\kappa-\varepsilon$ turbulence model in this particular case). Contours for these two variables are shown in Figs. 11 and 12.

Results for turbulent kinetic energy and dissipation rate found in this research are similar to those presented in other papers [10,21] from different researchers. Comparing kinetic energy contours for water–air [11] and water–air–solid [10] mixtures to those shown in Fig. 12, it is noticed that the highest values are found closer to the sparger as the solid volume fraction increases.

In water–air simulation [11], the highest values for the specific turbulent kinetic energy were reported to be around $1 \times 10^{-2}\,\mathrm{m}^2/\mathrm{s}^2$, while [10] for water–air–solids reached values around $5 \times 10^{-2}\,\mathrm{m}^2/\mathrm{s}^2$. Hence, the increasing effect is attributed to the presence of the dispersed solid phase. When there are three phases in the system, it is expected to find specific kinetic energy values between the two mentioned above due to the presence of a dispersed solid phase at a volume fraction in between. Therefore, the magnitude of $1.5 \times 10^{-2}\,\mathrm{m}^2/\mathrm{s}^2$ obtained in this modeling is in agreement with previous research.

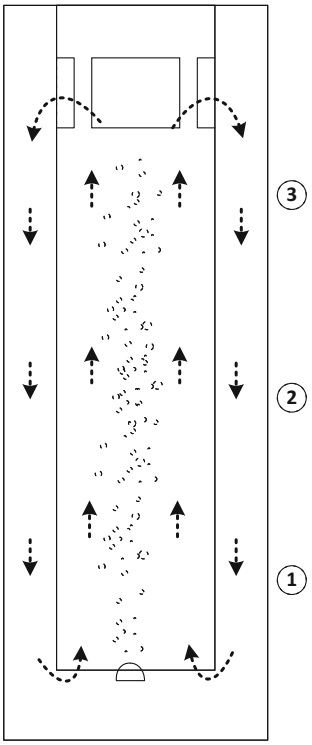

Fig. 13 Measurement points at the PBR

Table 7 Actual water velocity

Point #	Experimental velocity (m/s)	Simulated velocity (m/s)	%Error
1	0.1702	0.1585	6.86
2	0.1930	0.1579	18.20
3	0.1839	0.1599	13.05

Turbulent kinetic energy and turbulent dissipation rate reach their highest values at the top and middle section of the riser, while the downcomer presents the lowest magnitudes, confirming that phase interactions could influence the kinetic energy and turbulent dissipation rate distribution.

5 Experimental validation

5.1 Velocity measurement

Experimental validation in the PBR (32 l in capacity) was performed using an ultrasonic mass flowmeter. The sensor was placed on the external wall of the equipment in order to measure the velocity of the multiphase mixture between the two concentric cylinders. For this experimental setup, the sensor was located at three different points as shown in Fig. 13. Multiple repetitions were made, and the final results are presented in Table 7. Values for velocity from the CFD simulation are presented as well.

5.2 Air plume oscillation

A total of 30 s of the PBR's operation was simulated using the present CFD model. A time step of 0.1 s was used, in order to capture the fast-changing transient process at the beginning of the simulation.

Figure 14 compares the behavior of the air plume during the simulation, with the dynamic of the real multiphase flow. It is important to point out that the CAD used during the simulation has been adjusted to fit the level reached by water in the photobioreactor (close to the middle of circulation windows).

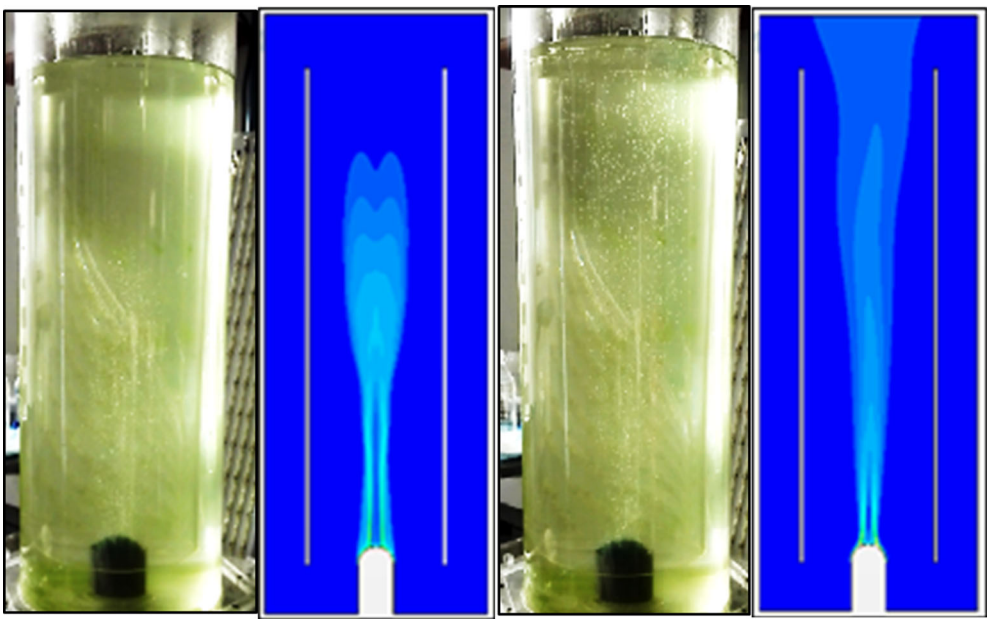

Fig. 14 PBR experimental and CFD results at $t = 1$ s (*left*), $t = 7$ s (*right*)

After 1 s, air bubbles have started to rise in the PBR. After 7 s, the air phase reaches the top of the riser and the air plume begins to oscillate, as shown in Fig. 14. According to these results, there is a suitable agreement between computational predictions and experimental behavior of the system.

From the presented results, in which some hydrodynamic variables of the process were studied, it is feasible to have a reference point to start an optimization for the operation of the PBR for microalgae culture.

6 Conclusions

A two-dimensional CFD model was used to simulate the multiphase flow in an airlift photobioreactor. According to the results, the mathematical model employed for describing the hydrodynamic variables leads to accurate predictions when compared to experimental behavior. From air volume fraction contours, it is evident that the riser has a higher presence of bubbles, with volume fraction close to zero in the downcomer. This characteristic allows the continuous phase as well for microalgae to have a complete recirculation at the specified inlet air volumetric flow. However, it is observed that microalgae cells have a slight accumulation at the lower section of the downcomer. This could be a consequence of the quasi-stagnation condition found at this area. Design improvements might be accomplished in order to avoid this phenomenon. Evidence showed microalgae sedimentation at that region of the actual PBR.

From the kinetic behavior of microalgae, we conclude that because of the small size of the microorganisms, they follow the water velocity vectors and describe a flow pattern similar to that of the continuous phase.

Turbulent kinetic energy and turbulent dissipation rate have similar distribution along the photobioreactor. Both of them exhibit their highest magnitudes at the top and at the middle regions of the riser, which indicates that the interactions among the phases have an influence on the distribution of these two variables.

These results, supported by the experimental observation, demonstrate that simulation is a powerful tool for a thorough comprehension of the photobioreactor behavior, and that it could be used to visualize operation conditions with higher cell density that obstructs optical devices. That is especially important when considering that an average photobioreactor should yield a biomass density thirty times higher than that used in our experiment.

Visualization of the operation conditions might also be useful for improving photobioreactor design. Modeling techniques could be used to eliminate dead zones like those found in the bottom of the reactor. A smaller and more efficient reactor might be achieved with minimum construction costs.

Acknowledgements This paper is the result of the research project Implementation of R & D (Microalgae components) to promote development and technology transfer in the agroindustrial production in Departamento del Atlántico, which is funded by Departamento del Atlántico through resources from Sistema General de Regalías–Fondo de Ciencia, Tecnología e Innovación (Grant no. FOESPC 52603 PR0004 Algas).

References

1. Benavente-Valdés, J., Montañez, J., Aguilar, C., Méndez-Zavala, A., Yaldivia, B.: Tecnología de cultivo de microalgas en fotobiorreactores. Revista Científica de la Universidad Autónoma de Coahuila. **7**(4), 1–12 (2012)
2. Bitog, J., Lee, I., Lee, C., Kim, K., Hwang, H., Hong, S.: Application of computational fluid dynamics for modeling and designing photobioreactors for microalgae production: a review. Comput. Electron. Agric. **76**(2), 131–147 (2011)
3. Pulz, O.: Photobioreactors: production systems for phototrophic microorganisms. Appl. Microbiol. Biotechnol. **57**(3), 287–293 (2001)
4. Xu, L., Rui, L., Feng, W., Chun-Zhao, L.: Development of a draft-tube airlift bioreactor for *Botryococcus braunii* with an optimized inner structure using computational fluid dynamics. Bioresour. Technol. **199**, 300–305 (2012)
5. Roy, S., Dhotre, M., Joshi, J.: CFD simulation of flow and axial dispersion in external loop airlift reactor. Chem. Eng. Res. Des. **84**(8), 677–690 (2006)
6. Pollard, D., Ison, A., Shamalou, P., Lilly, M.: Reactor heterogeneity with saccharopolyspora erythraea airlift fermentations. Biotechnol. Bioeng. **58**(5), 453–463 (1998)
7. Contreras-Flores, C., Peña-Castro, J., Flores-Cotera, L., Cañizares-Villanueva, R.: Advances in conceptual design of photobioreactors for microalgal culture. Interciencia **28**(8), 450–456 (2008)
8. Razzak, S., Hossaina, M., Rahima, A.: Integrated CO_2 capture, wastewater treatment and biofuel production by microalgae culturing—a review. Renew. Sustain. Energy Rev. **27**, 622–653 (2013)
9. Hutmacher, D., Singh, H.: Computational fluid dynamics for improved bioreactor design and 3D culture. Trends Biotechnol. **26**(4), 166–172 (2008)
10. Oey, R., Mudde, R., Portela, L., Van Den Akker, H.: Simulation of a slurry airlift using a two-fluid model. Chem. Eng. Sci. **56**(2), 673–681 (2001)
11. García, S., Paternina, E., Pupo, O., Bula, A., Di Mare, L.: CFD simulation of multiphase flow in an airlift column photobioreactor. Glob. NEST J. **16**(6), 1121–1134 (2014)
12. Luo, H., Al-Dahhan, M.: Local characteristics of hydrodynamics in draft tube airlift bioreactor. Chem. Eng. Sci. **63**(11), 3057–3068 (2008)
13. Wang, X., Jia, X., Wen, J.: Transient CFD modeling of toluene waste gas biodegradation in a gas–liquid–solid three-phase airlift loop reactor by immobilized pseudomonas putida. Chem. Eng. J. **172**(2–3), 735–745 (2011)
14. Luo, H., Al-Dahhan, M.: Verification and validation of CFD simulations for local flow dynamics in a draft tube airlift bioreactor. Chem. Eng. Sci. **66**(5), 907–923 (2011)
15. Jones, W., Launder, B.: The prediction of laminarization with a two-equation model of turbulence. Int. J. Heat Mass Transf. **15**(2), 301–314 (1972)
16. Launder, B., Sharma, B.: Application of the energy-dissipation model of turbulence to the calculation of flow near a spinning disc. Lett. Heat Mass Transf. **1**(2), 131–137 (1974)
17. Pfleger, D., Gomes, S., Gilbert, N., Wagner, H.: Hydrodynamic simulations of laboratory scale bubble columns fundamental studies of the Eulerian–Eulerian modelling approach. Chem. Eng. Sci. **54**(21), 5091–5099 (1999)
18. CD-Adapco.: STAR-CCM+ User Guide, Version 8.02. CD-Adapco, New York (2013)
19. Prochazkova, G., Petr, K., Branyik, T.: Harvesting freshwater chlorella vulgaris with flocculant derived from spent brewer's yeast. Bioresour. Technol. **177**, 28–33 (2015)
20. Lampert, W., Sommer, U.: Limnoecology: The Ecology of Lakes and Streams. Oxford University Press, New York (1997)
21. Liu, R., Liu, Y., Liu, C.: Development of an efficient CFD-simulation method to optimize the structure parameters of an airlift sonobioreactor. Chem. Eng. Res. Des. **91**, 211–220 (2013)